# Supplementary Information for

## Tailored nanoscale plasmon-enhanced vibrational electron spectroscopy

Luiz H. G. Tizei,[1,*] Vahagn Mkhitaryan,[2] Hugo Lourenço-Martins,[1] Leonardo Scarabelli,[3,4] Kenji Watanabe,[5] Takashi Taniguchi,[5] Marcel Tencé,[1] Jean-Denis Blazit,[1] Xiaoyan Li,[1] Alexandre Gloter,[1] Alberto Zobelli,[1] Franz-Philipp Schmidt,[6] Luis M. Liz-Marzán,[3,7] Javier García de Abajo,[2,8] Odile Stéphan,[1] and Mathieu Kociak[1,†]

1. Laboratoire de Physique des Solides, Université Paris-Sud, CNRS-UMR 8502, Orsay 91405, France
2. ICFO-Institut de Ciencies Fotoniques, The Barcelona Institute of Science and Technology, 08860 Castelldefels (Barcelona), Spain
3. CIC biomaGUNE and Ciber-BBN, Paseo de Miramón 182, 20014 Donostia-San Sebastián, Spain
4. Department of Chemistry and Biochemistry, University of California, Los Angeles, Los Angeles, California 90095, USA
5. National Institute for Materials Science, Namiki 1-1, Tsukuba, Ibaraki 305-0044, Japan
6. Institute of Physics, University of Graz, Universittsplatz 5, 8010 Graz, Austria
7.Ikerbasque, Basque Foundation for Science, 48013 Bilbao, Spain
8.ICREA-Institució Catalana de Recerca i Estudis Avanats, Passeig Lluís Companys 23, 08010 Barcelona, Spain

Correspondence to: luiz.galvao-tizei@u-psud.fr; mathieu.kociak@u-psud.fr

**This PDF file includes:**

## Materials and Methods

### Electron spectroscopy and microscopy

Experiments were performed on a modified Nion Hermes200 (known as ChromaTEM) equipped with an electron monochromator, an optimized electron spectrometer (Nion Iris), and a cold field emission electron gun. The NION Iris spectrometer was equipped with a Princeton Instrument Kuros camera. The electron beam used had a kinetic energy of 60 keV, an energy resolution (defined as the full width at half maximum (FWHM) of the zero-loss peak) between 6 and 10 meV (this value was optimized and controlled after each acquisition), a current intensity between 5 and 20 pA, a convergence half-angle of 10 mrad, and a FWHM in real space of about 1 nm. The spectrometer was set to have a diffraction pattern at its entrance (image coupling mode) and a 1 mm entrance aperture was used to collect electrons up to 15 mrad (half-angle). All data were acquired as hyperspectral images, with two spatial dimensions (electron beam scan in real space) and one energy loss dimension. All peak positions are reported with an error of ± 5 meV, which include errors due to background subtraction.

### Sample preparation

The synthesis follows the protocol reported by Mayer et al. In 2015 [Ref. 19]. In order to proceed with the growth of AgAuAg bimetallic nanowires, it is necessary to synthetize penta-twinned gold nanorods to be used as cores for the epitaxial deposition of silver. The synthesis of this material can be found in the literature.[20]

**Materials.** Benzyldimethylhexadecylammonium chloride (BDAC), silver nitrate (AgNO3, ≥ 99.9%), L-ascorbic acid (AA, ≥ 99%), were purchased from Aldrich. All chemicals were used as received. Milli-Q water (resistivity 18.2 MΩcm at 25 °C) was used in all experiments. All glassware was washed with aqua regia, rinsed with water, and dried before use.

**AgAuAg bimetallic nanowires synthesis.** 20 mL of the purified Penta-Twinned Au Nanorod solution was heated to 60 °C using an oil bath. A AgNO3 solution (0.004 M in water) and an AA solution (0.016 M in 20 mM BDAC) were prepared and loaded into separated syringes. Using a syringe pump, both AgNO3 and AA were added to the Penta-Twinned Au Nanorod solution at a rate of 300 μL/h (0.24 mol of Ag(I) per mol of Au(0) per hour) under slow stirring keeping the temperature constant at 60 °C. The growth of the nanowires was monitored through UV-vis-NIR spectroscopy on a small sample (1 mL) periodically withdrawn from the growing solution. To obtain AgAuAg nanowires above 3 μm in length (average 3.4 ± 0.6 μm for the specific sample used in this manuscript), the growth was continued for 72 hours.

### Metallic nanowire and *h*-BN milling

Metallic nanowire and *h*-BN milling was performed on a JEOL 2010 electron microscope equipped with a thermionic electron gun ($LaB_6$ crystal). This kind of microscope was chosen to ensure the maximum total current available in the focused electron beam (in contrast to the maximum current density, which would be achieved with a cold field emission gun). Most

efficient milling was achieved with 200 keV kinetic energy electrons and a beam extraction current between 10 and 15 μA.

Milling of the two materials was achieved through different mechanisms. Ag atoms are heavy and energy conservation prevents efficient atoms removal by momentum transfer. For this reason, large currents were used to heat the material and diffuse atoms away from the target area. Because of this, milling was quite dependent on the underlying substrate. The highest precision was achieved with nanowire parts on vacuum, followed by milling on *h*-BN. On the carbon support film, milling was less favorable, probably due to good heat conductivity of the film. B and N atoms are light and are easily removed by direct momentum transfer from the electron beam. This intuitive description might undergo corrections due to atom removal due to electronic transitions to antibonding orbitals as an additional mechanism different from knock-on electron-nucleus impact.

## Data analysis

Data acquisition and initial check were performed using Nion Swift and in-house Kuros driver. Data analysis was performed with Python libraries: Hyperspy, Numpy, Matplotlib and Scipy. Spectra were fitted with multiple Gaussians, unless otherwise noted.

## Sample preparation

Samples were prepared by sequentially solutions drop casting containing the metallic nanowires and *h*-BN flakes (chemically exfoliated in IPA). Nanowires where chosen by inspection in an electron microscope considering their length and the quantity of *h*-BN underlying them.

## Purcell factor calculations

In order to better understand the experimental measurements in a quantitative fashiion, we present numerical simulations of the optical response of our system (Ag nanowires on top of h-BN thin films) carried out by using a finite-difference-time-domain (FDTD) method. In these simulations, plasmon modes are excited by an electric dipole source placed near the end of the nanowire, at a position away from high-symmetry points in order to guarantee a nonzero electric field of the plasmon standing wave, and therefore, a high excitation efficiently. We exploit the proportionality between the EELS probability and the local density of electromagnetic states (LDOS)[27]

$$\Gamma_{EELS}=\frac{-2\pi e^2}{\hbar\omega}\rho_z\left(R_0,q_v,\omega\right),$$

where $e$ is the elementary charge, $\omega$ is the frequency of the electromagnetic field, $q_v=\omega/v$, and $v$ is the electron velocity. Here, $\rho_z\left(R_0,q,\omega\right)$ is the projected LDOS (along the direction of the electron trajectory, which is taken along the $z$ axis) at the in-plane position $R_0=\left(x_0,y_0\right)$ of the

electron trajectory and evaluated in wave vector space along the *z* direction. Instead of this quantity, we compute the LDOS in real space along *z*, which is in turn proportional to the so-called Purcell factor (i.e., the enhancement of the decay rate $\gamma$ of a dipole emitter placed at the position of interest, compared with the free space decay rate $\gamma_0$). More precisely,[28]

$$P=\frac{\gamma}{\gamma_0}=\frac{2\pi c^2}{\omega^2}\rho_z(R_0,z,\omega),$$

Although the LDOS in two the expressions above are not equivalent, we argue that both plasmons and polaritons are extremely localized in space, both of them should produce similar spectral profiles, and, for simplicity, we use the second one, which is more direct to compute in our method.

Strong coupling

Experimental data display a clear avoided crossing behavior indicative of strong coupling between the plasmon and phonon modes. To characterize the coupling strength, we model the system using a simple model based upon two coupled harmonic oscillators. Despite its simplicity, this model is capable of capturing the main characteristics of the coupling. The hybrid system has oscillation frequencies

$$\omega_{\pm}(q)=\frac{1}{2}(\omega_{pl}+\omega_{ph})\pm\sqrt{\frac{1}{4}(\omega_{pl}-\omega_{ph})^2+g^2},$$

where $\omega_{pl}$ is the plasmon frequency, $\omega_{ph}$ is the phonon frequency, and $g$ is the strength of the coupling between the two modes. The latter serves as a parameter to fit the experiment using the analytically calculated plasmon dispersion $\omega_{pl}(q)$ of the infinite nanowire and the phonon dispersion $\omega_{ph}(q)$ of the h-BN thin film.

The plasmon dispersion in an infinitely long nanowire is given with the expression[29]

$$\frac{mq^2}{a^2}\left(\frac{1}{k_{2\perp}^2}-\frac{1}{k_{1\perp}^2}\right)^2=\left[\frac{1}{k_{2\perp}}\frac{J_m'(k_{2\perp}a)}{J_m(k_{2\perp}a)}-\frac{1}{k_{1\perp}}\frac{H_m^{(1)\prime}(k_{1\perp}a)}{H_m^{(1)}(k_{1\perp}a)}\right]\times\left[\frac{k_2^2}{k_{2\perp}}\frac{J_m'(k_{2\perp}a)}{J_m(k_{2\perp}a)}-\frac{k_1^2}{k_{1\perp}}\frac{H_m^{(1)\prime}(k_{1\perp}a)}{H_m^{(1)}(k_{1\perp}a)}\right],$$

where *a* is the wire radius, *m* is the azimuthal order of the plasmon (*m*=0 in our case), $k_j=\epsilon_j k_0$, $k_0=\omega/c$, and $k_{j\perp}=\sqrt{k_j^2-q^2}$ is the transverse wave vector in medium *j*, with *j=1,2* referring to vacuum and silver.

The phonon-polariton modes of the *h*-BN film are calculated from the Fresnel reflection coefficient. In particular, for Fig. 14A we use the imaginary part of the reflection coefficient for the *p* polarized fields $\Im\{r_p\}$, which readily gives the hyperbolic phonon-polaritonic bands (KF modes). In Fig. 14B, we compare the coupling strength with the plasmon and phonon resonance widths that are again extracted from simulations. It is clear that the coupling strength is larger than the plasmon and phonon widths for small values of *q*, therefore indicating that the system undergoes strong coupling.

**Supplementary figures**

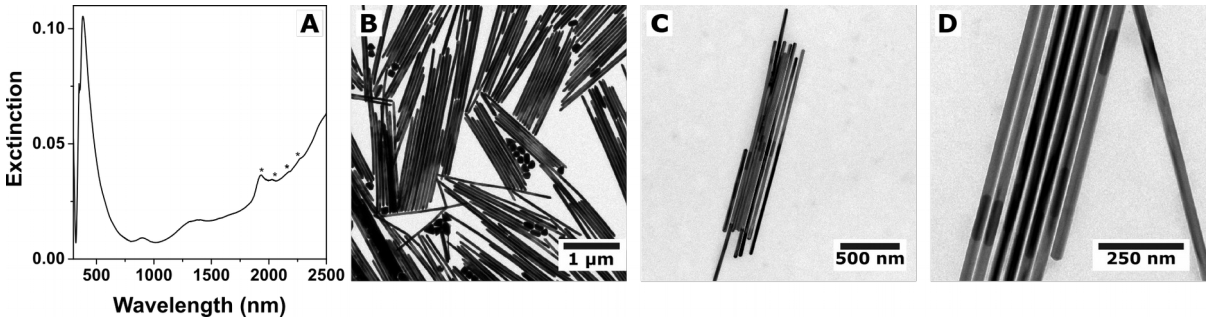


**Fig. 1. Characterization of AgAuAg bimetallic nanowires. (A)** UV-vis-NIR spectra of a colloidal suspension of the nanowires used in this study, taken in deuterated water. Asterisks indicate residual water peaks. **(B-D)** TEM images taken at different fileds of view. In panel D, the gold cores are clearly visible.

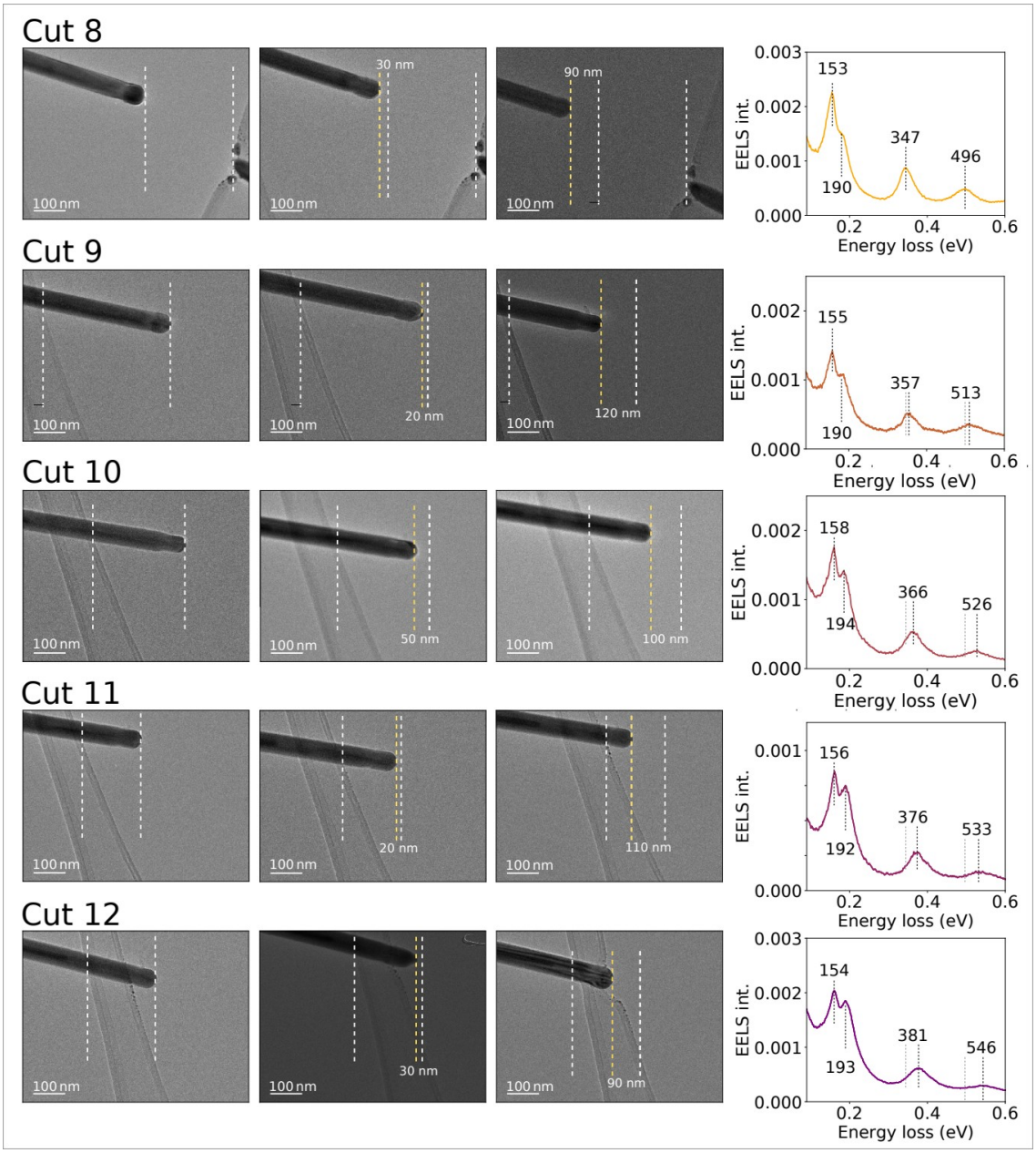


**Fig. 2 Plasmon tuning by nanowire shapping.** The three panels on the left of each line show TEM images at initial (lef), intermediary (middle) and final (right) steps of cuts 8, 9, 10, 11, and 12 of the nanowire presented in Fig. 2 of the main text. White lines are guides to the eye. In the right panel, corresponding spectra measured at the tip are shown. Their energy positions are displayed in milli-electronvolts and were extracted from multi-Gaussian curve fitting to the data. Dotted lines are guides to the eye and grey lines mark their original positions in cut 8. The quadrupolar and sextupolar modes (initially at 347 and 496 meV) disperse to higher energy as expected for plasmon modes. The two strongly-coupled modes (initially at 153 and 190 meV) do not disperse within our measured precision in the explored length range.

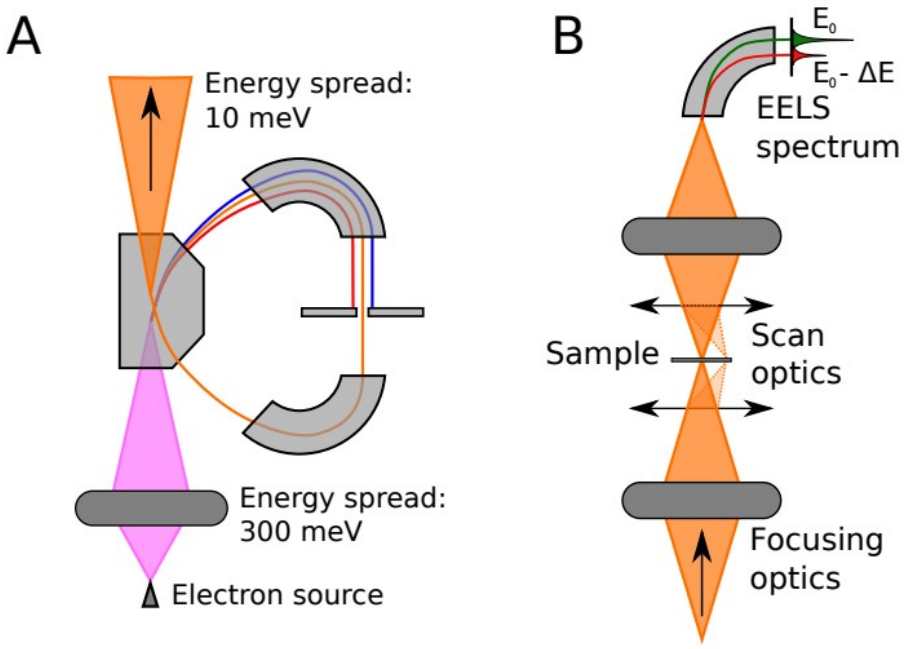


**Fig. 3. General description of the experimental configuration. (A)** An electron monochromator is used to reduce the energy width of a free electron beam down to 5-10 meV. **(B)** An electron microscope focuses the monochromated electron beam down to subnanometer sizes. The focused beam is scanned in real space to construct energy-resolved maps of the samples.

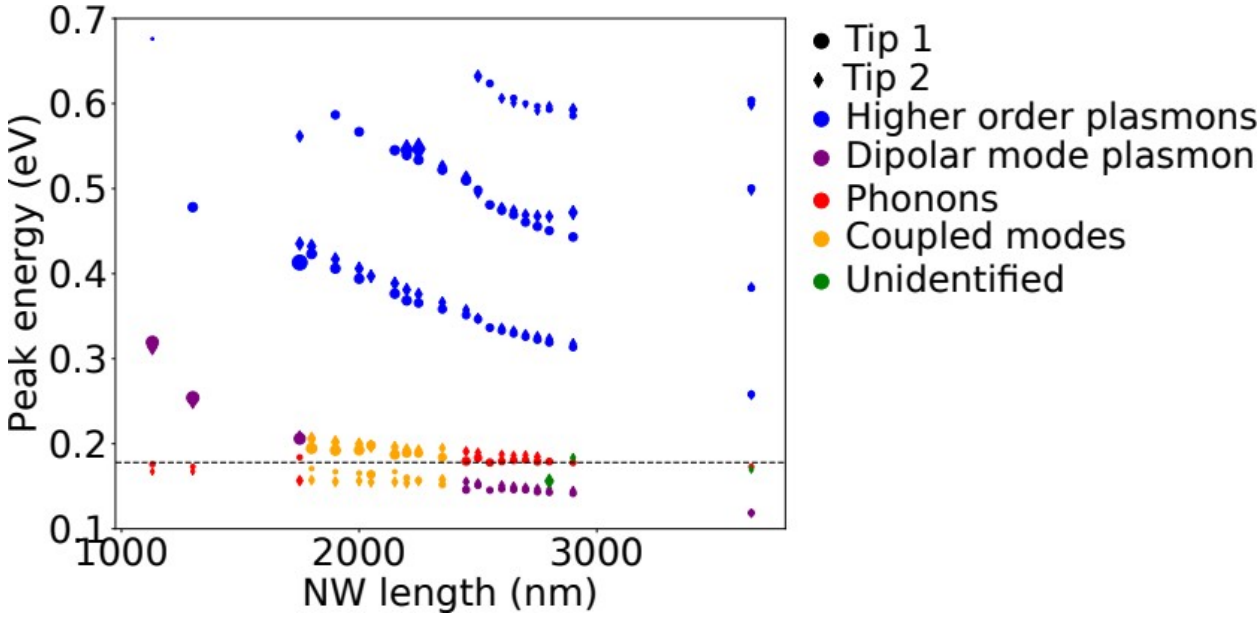


**Fig. 4. Dispersion of the higher-order plasmon modes versus energy.** The distinction between the dipolar plasmon mode/phonons and coupled modes is only intended a guides to the eye.

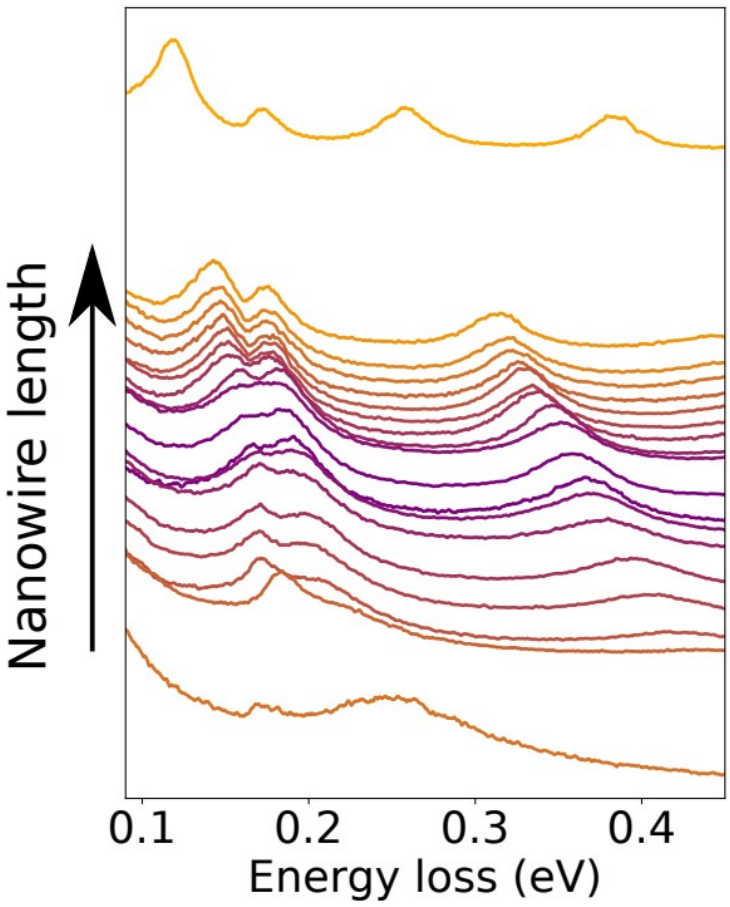


**Fig. 5. Spectra measured on tip 1 (on *h*-BN) of the nanowire presented in Fig. 2 of the main text.**

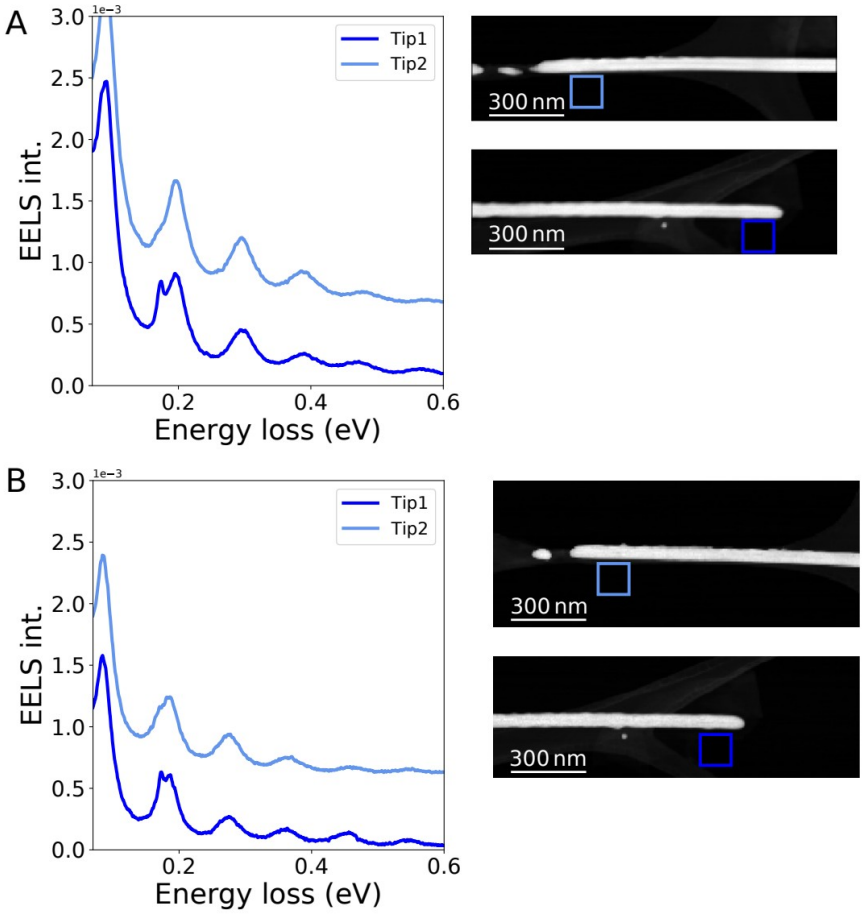


**Fig. 6. Nanowire with small amount of *h*-BN and no coupling. (A)** and **(B)** show EELS spectra measured at tips 1 (dark blue; tip close to *h*-BN) and 2 (light blue, tip far from *h*-BN) of the same nanowire with different lengths. The plasmon mode at around 180 meV disperses as a function of length and does not show peak splitting (the two observed peaks are the expected ones for *h*-BN, superimposed on the nanowire dipolar plasmon peak), which is the behavior expected for the uncoupled system.

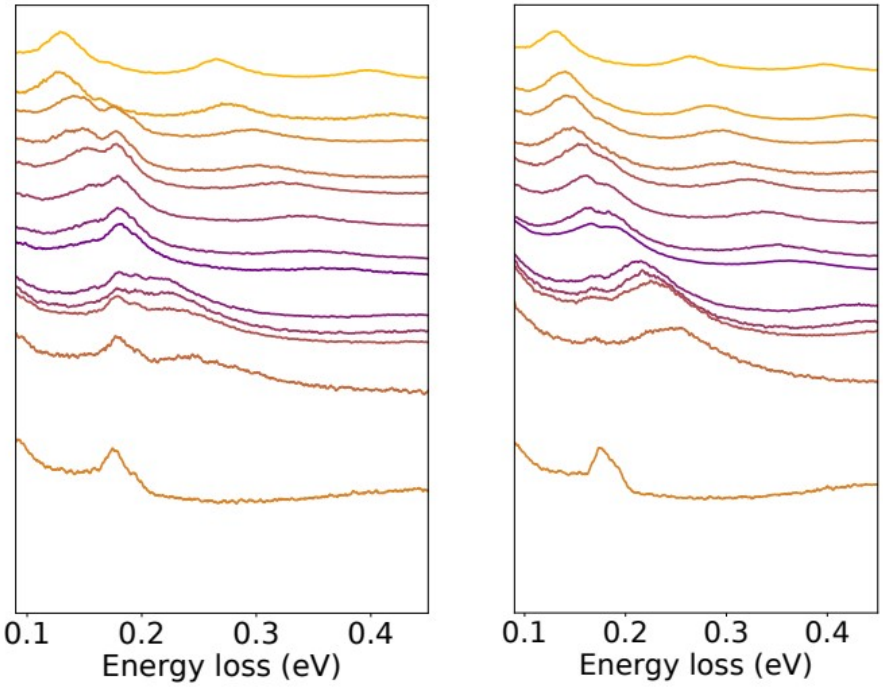


**Fig. 7. Nanowire with intermediate amounts of h-BN, resulting in 17 meV splitting.**

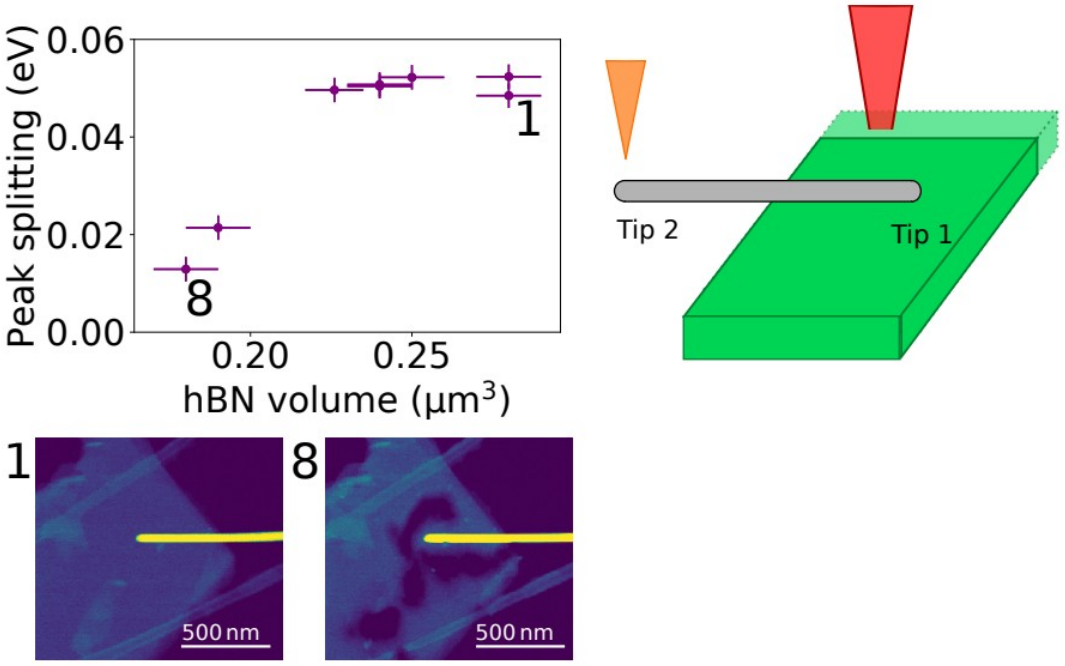


**Fig. 8. Coupling strength as a function of *h*-BN volume close to the nanowire tip.** The splitting of the two strongly-coupled modes of a nanowire changes as a function of the *h*-BN volume present on the other tip of the nanowire. The volume was measured within 500 nm of the nanowire tip. For this specific nanowire, the splitting changed from 57 meV to 12 meV. The change in the projection of the *h*-BN volume between steps 1 and 8 is shown in the images in the bottom marked 1 and 8. Milling of *h*-BN was performed using a 200 keV high current (μA) beam in a conventional TEM.

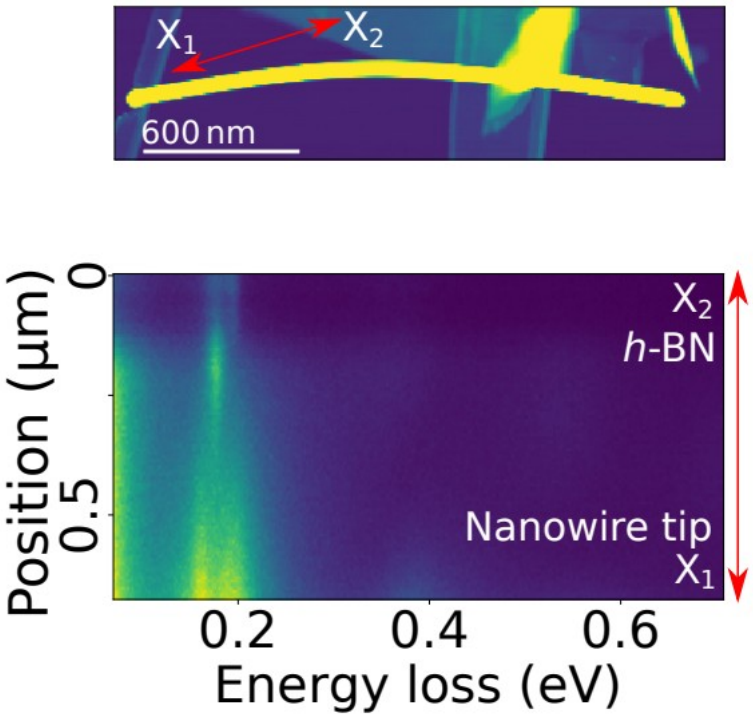


**Fig. 9. Spatial-spectral evolution around the tip of the nanowire when strong coupling occurs.** Spatial evolution of the EELS intensity when moving the electron beam from the tip of the nanowire toward and into the *h*-BN flake along the red double arrow marked X1-X2. The two strongly coupled modes lose intensity away from the nanowire tip as the aloof spectra of *h*-BN appears. With the electron beam in *h*-BN, the two Fuchs-Kliewer modes are observed.

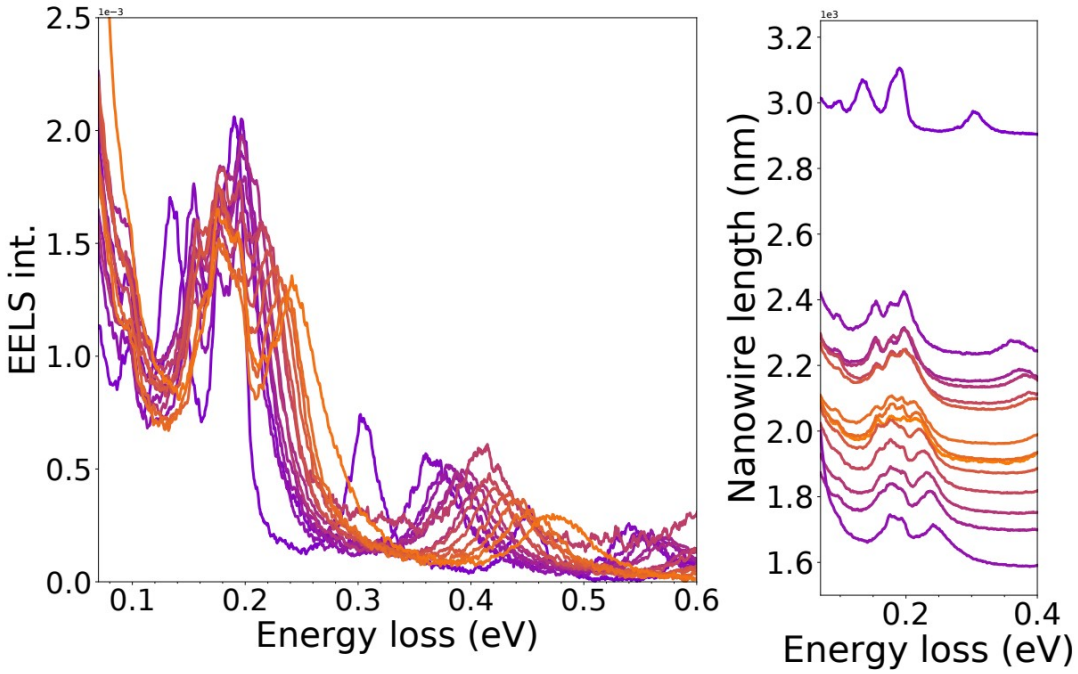


**Fig. 10. Spectral evolution for all lengths of the nanowire on *h*-BN used in Fig. 3 of the main text.** The nanowire length increases towards the top from 1.6 μm to 2.9 μm. The left panel shows all of the spectra superimposed and the right panel offset based on the nanowire length.

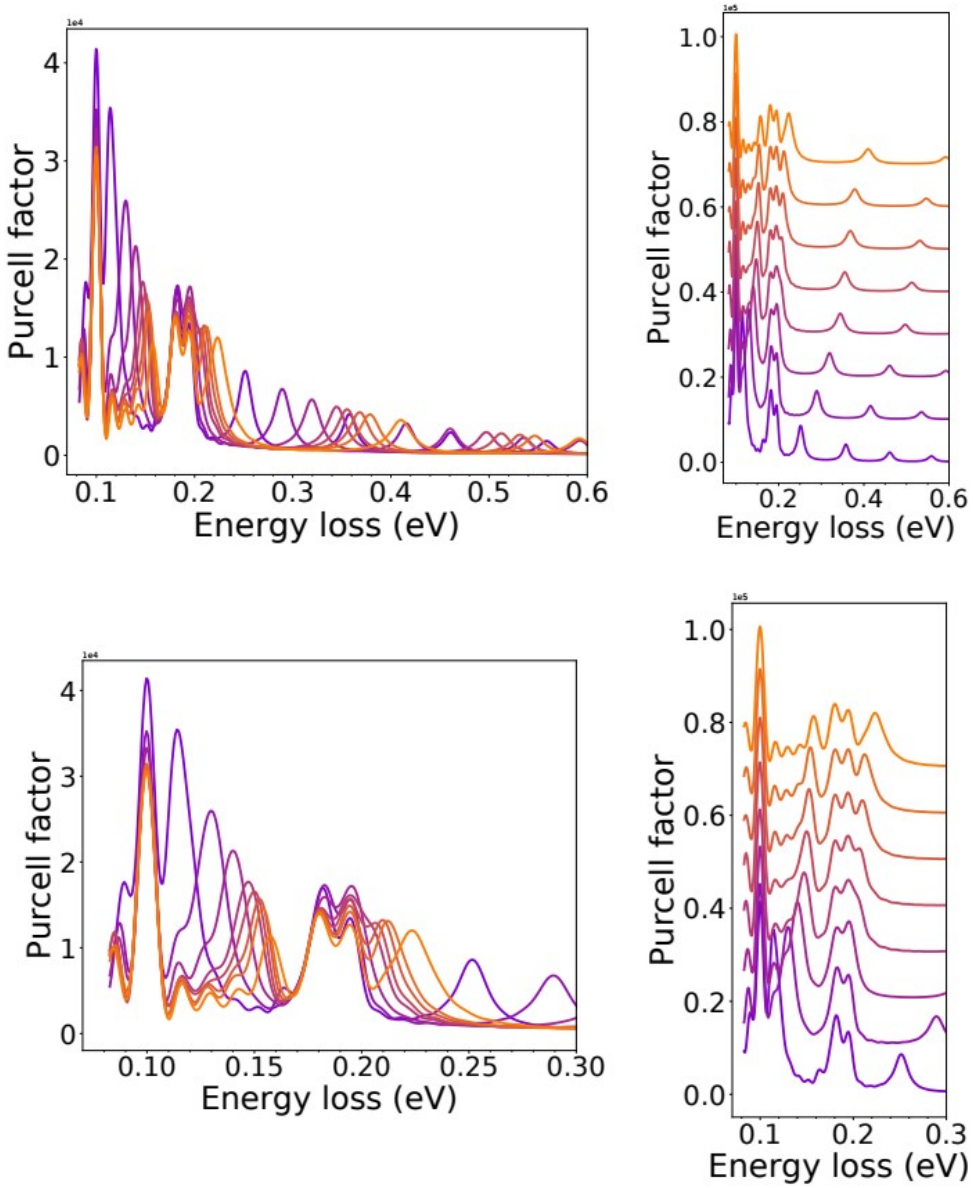


**Fig. 11. Numerical calculations of the Purcell factor due to a Ag nanowire placed on a 50 nm thick *h*-BN layer.**

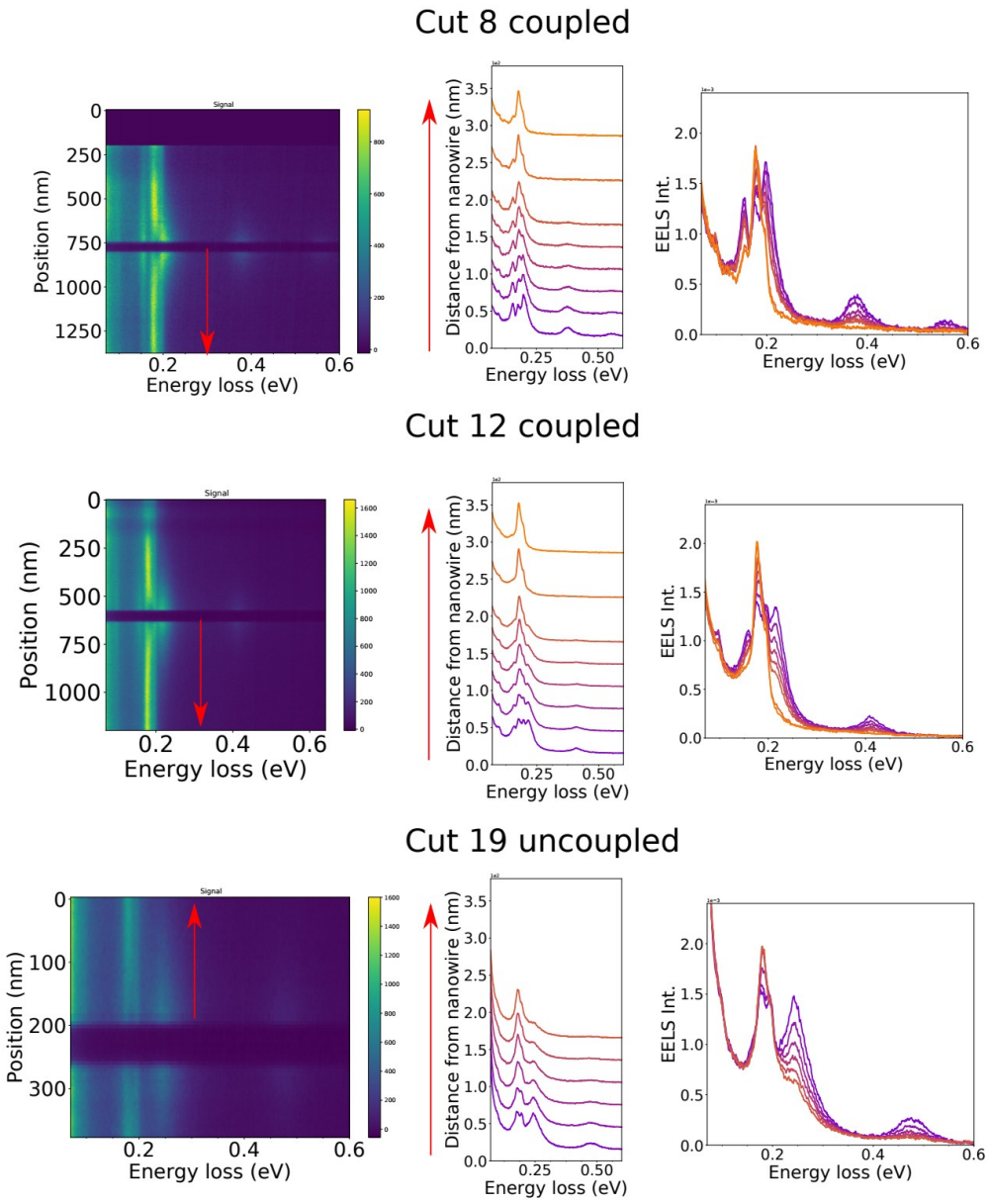


**Fig. 12. Spectral evolution away from the surface of the nanowire for different nanowire lengths.** The left panel shows a 2D map of the EELS intensity as a function of energy loss and distance to the nanowire. The latter is positioned at the dark bands in the center of each panel. The center and left panel show the spectral evolution as a function of distance for selected distances with and without an offset (given by the distance), respectively.

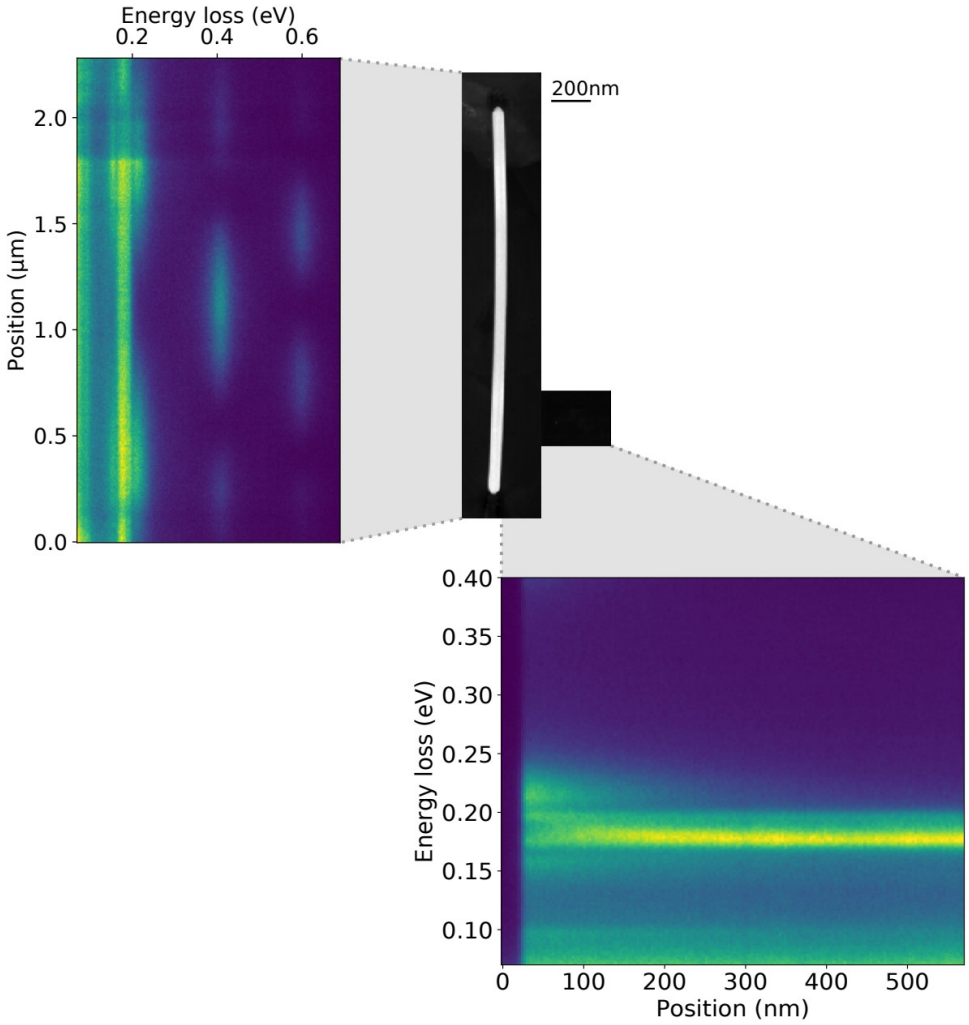


**Fig. 13. Hyperspectral image projection along and across the nanowire axis.** On the upper right (along the nanowire axis) projection, one can clearly observe close to the tips the presence of the ZO, PPA, and PPS modes, while at the center they fade and only the ZO mode remains (in addition to the *h*-BN normal signature). At higher energies two other plasmons are observed. On the lower left plot, a projection along the perpendicular direction is shown. Here, the decay of the ZO, PPA, and PPS modes away from the surface are resolved. This effect is clearer on the fitted intensity curves shown in Fig. 3d of the main text.

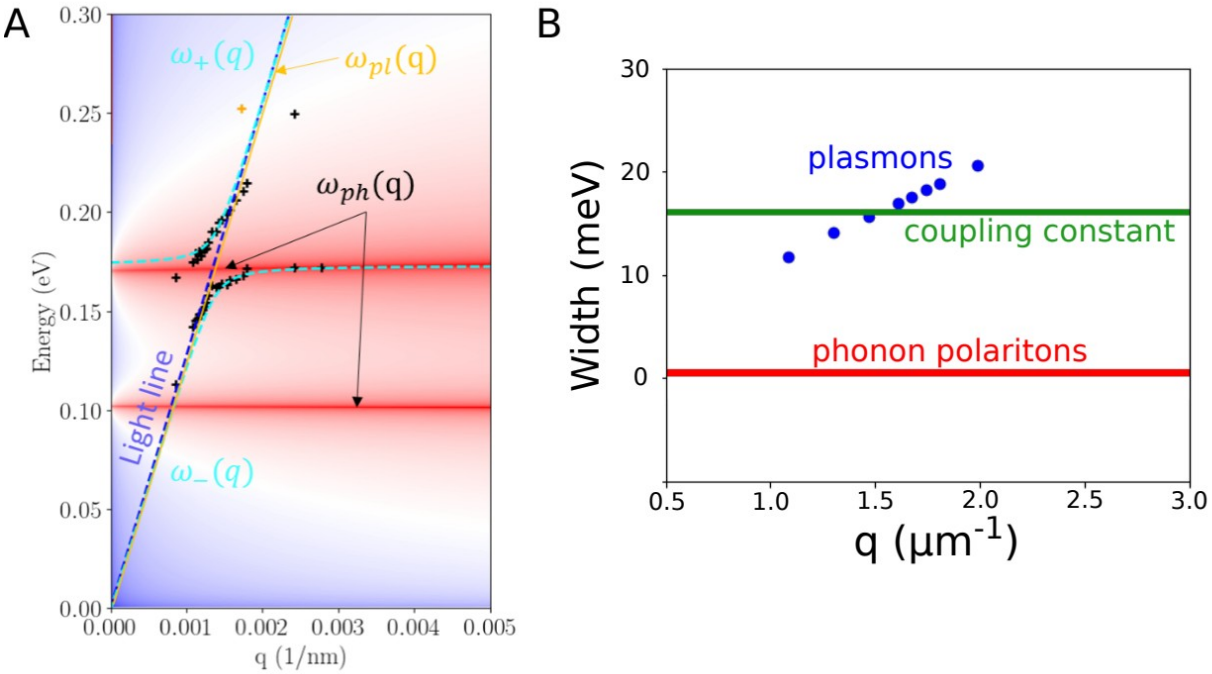


**Fig. 14. Strong coupling regime calculations. (A)** Strong coupling calculation between plasmon and phonon modes, as described in the methods above. **(B)** Comparison of the coupling strength *g* to the plasmon and phonon widths extracted from the simulations.